JACS
JOURNAL OF THE AMERICAN CHEMICAL SOCIETY

Article

pubs.acs.org/JACS

The Formation Time of Ti−O• and Ti−O•−Ti Radicals at the n-$SrTiO_3$/Aqueous Interface during Photocatalytic Water Oxidation

Xihan Chen,[†] Stephanie N. Choing,[†] Daniel J. Aschaffenburg,[†] C. D. Pemmaraju,[‡] David Prendergast,[§] and Tanja Cuk*[,†,‡]

[†]Department of Chemistry, University of California, Berkeley, Berkeley, California 94720, United States

[‡]Chemical Sciences Division and [§]Molecular Foundry, Lawrence Berkeley National Laboratory, Berkeley, California 94720, United States

Supporting Information

ABSTRACT: The initial step of photocatalytic water oxidation reaction at the metal oxide/aqueous interface involves intermediates formed by trapping photogenerated, valence band holes on different reactive sites of the oxide surface. In $SrTiO_3$, these one-electron intermediates are radicals located in Ti−O• (oxyl) and Ti−O•−Ti (bridge) groups arranged perpendicular and parallel to the surface respectively, and form electronic states in the band gap of $SrTiO_3$. Using an ultrafast sub band gap probe of 400 nm and white light, we excited transitions between these radical states and the conduction band. By measuring the time evolution of surface reflectivity following the pump pulse of 266 nm light, we determined an initial radical formation time of 1.3 ± 0.2 ps, which is identical to the time to populate the surface with titanium oxyl (Ti−O•) radicals. The oxyl was separately observed by a subsurface vibration near 800 cm^{-1} from Ti−O located in the plane right below Ti−O•. Second, a polarized transition optical dipole allows us to assign the 1.3 ps time constant to the production of both O-site radicals. After a 4.5 ps delay, another distinct surface species forms with a time constant of 36 ± 10 ps with a yet undetermined structure. As would be expected, the radicals' decay, specifically probed by the oxyl's subsurface vibration, parallels that of the photocurrent. Our results led us to propose a nonadiabatic kinetic mechanism for generating radicals of the type Ti−O• and Ti−O•−Ti from valence band holes based on their solvation at aqueous interfaces.

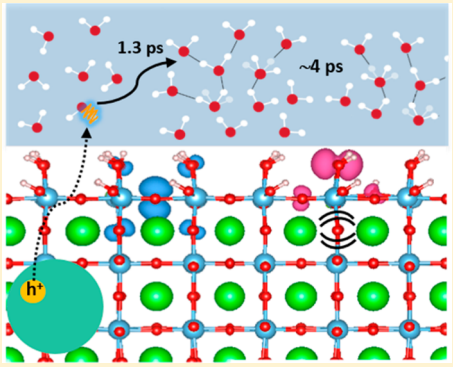

INTRODUCTION

For heterogeneous electrochemically or photoelectrochemically controlled catalysis, the initial step is the localization of charge into a one-electron intermediate at the surface.[1] For water oxidation at the transition metal oxide/aqueous interface, the one-electron intermediate derives from localization of a hole on either the metal or oxygen site and either in the plane of the surface or perpendicular to it.[2−5] For titania surfaces, calculations suggest two O-site radical species: the *out-of-plane* oxyl radical, Ti−O•, where the hole is localized on the O-site perpendicular to the plane, and the *in-plane* bridge radical, Ti−O•−Ti, where the hole is localized on the in-plane O-site. For the later transition metal oxides, such as iron and cobalt oxides, a metal oxo intermediate (e.g., Co(IV)═O, Fe(IV)═O), where the hole increases the oxidation state of the metal, is anticipated. The one-electron intermediate's particular electronic structure differentiates a catalyst's ability to facilitate O−O bond formation, thought to be the rate-limiting step in the catalytic cycle. Indeed, theoretical calculations of adsorption energies of OH* and O* species on transition metals scale with the activation energy of the O−O transition state.[6]

While these one-electron intermediates have been proposed for decades, only very recently have experiments been able to identify their electronic structure. Photoinitiated catalysis, where the intermediate is created by photogenerated holes, allows for the observation of their vibrations with a mid-infrared probe of the illuminated surface: the oxyl radical in titania (Ti−O•[7]) by the subsurface Ti−O vibration in the plane right below it and the metal oxo in iron oxide and cobalt oxide (Fe(IV)═O,[8] Co(IV)═O[9]) by the metal oxygen double bond.

In addition to the particular electronic structure of each one-electron intermediate, the distribution of two or more types at the heterogeneous surface is critical to catalytic activity. The charge transfer reaction of bulk charges to particular surface active sites regulates this distribution. For the photoinitiated water oxidation reaction, the intermediates arise from valence band holes. This process, which converts light energy into stable one-electron intermediates of water oxidation, represents a critical step of solar-to-fuel generation technologies that use water as a fuel-feedstock. In an effort to capture the charge-transfer reaction kinetics, several recent studies have applied time-resolved optical spectroscopy to the transition metal oxide/aqueous interface during photoelectrochemically controlled water oxidation. Thus, far, an optical signature of

Received: May 21, 2016
Revised: September 12, 2016
Published: December 7, 2016

ACS Publications © 2016 American Chemical Society

DOI: 10.1021/jacs.6b09550
J. Am. Chem. Soc. 2017, 139, 1830−1841

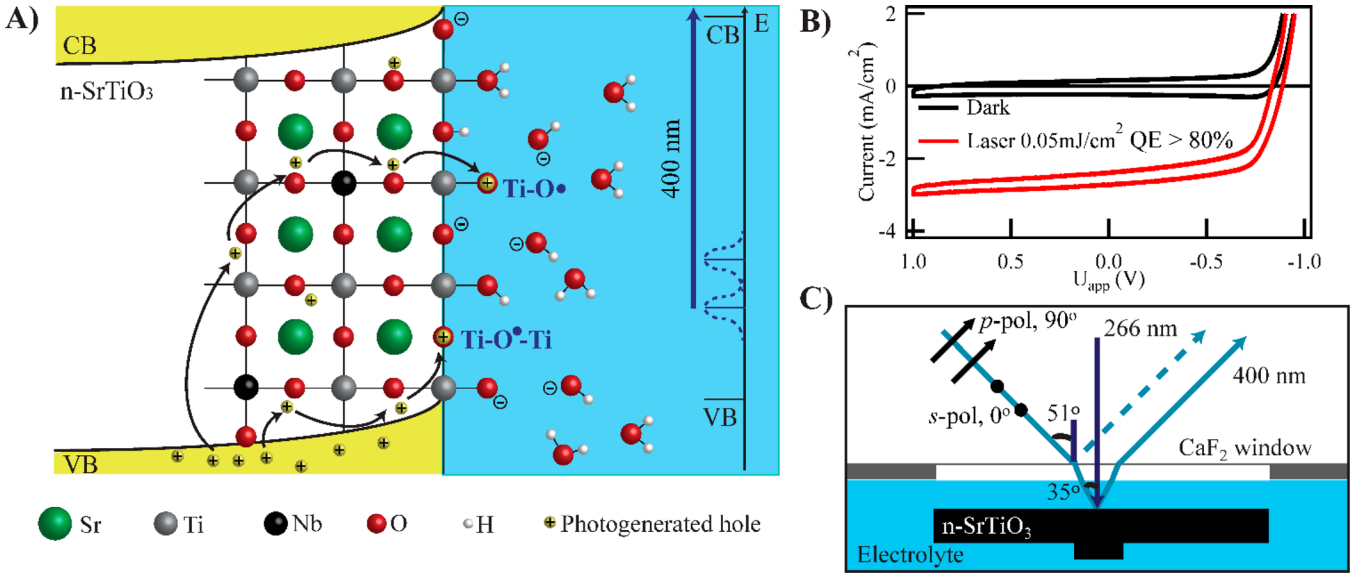

Figure 1. Representation of n-$SrTiO_3$ photoelectrode after bandgap (266 nm) photoexcitation. (A) Photoholes in the valence band of n-$SrTiO_3$ migrate to the surface to create O-site radicals: the titanium oxyl (Ti−O•) and the bridge (Ti−O•−Ti) radicals. These radicals create midgap states, whose optical transition to the conduction band minimum is excited by 400 nm light. (B) Cyclic voltammetry (CV) of the 0.1% Nb doped $SrTiO_3$ sample in the dark and illuminated by 266 nm, 500 Hz, 150 fs pulsed laser excitation (0.05 mJ/cm^2). A photon-to-current quantum efficiency greater than 80% is achieved. (C) A diagram of the *s*- or *p*- polarized 400 nm probe beam incident on the sample at an angle of 35° to the normal. The time-resolved reflectance change of the probe is measured after 266 nm excitation. See the detailed description in Figure S1A.

trapped surface holes at millisecond time scales decays with a third order dependence on the concentration of initially excited valence band holes, which suggests that O_2 evolution is rate-limited by a three-hole process involving surface bound intermediates.[10,11] On the other hand, at picosecond to nanosecond time scales, the decay of the valence band holes was observed.[12,13] As described for the n-$SrTiO_3$/aqueous interface,[13] the decay is potential dependent, such that the activation barrier for hole transfer to the surface lowers at more oxidative potentials (tuned by the applied voltage).

A crucial component of the charge-transfer reaction regulating the surface distribution is missing—the assignment of a formation time to a particular intermediate. At the surface of semiconductors, localized charge, which O-site radicals and metal oxo species are forms of, creates midgap states.[14,15] In principle, time resolving the formation of a midgap state during photoinitiated water oxidation assigns a formation time to an intermediate. Any spectroscopic signatures of the intermediates that are specific to its local electronic structure could significantly facilitate the assignment.

Here, we show that time-resolved reflectivity of the single crystal n-$SrTiO_3$/aqueous interface during water oxidation, probed by 400 nm and white light following a 266 nm pump pulse, reveals a formation time constant (1.3 ps) that stabilizes a distribution of both bridge (Ti−O•−Ti) and oxyl (Ti−O•) radical populations. The sub-band gap probe stimulates emission of conduction band electrons to the radicals' midgap states with a spectrum characteristic of photoluminescence from $SrTiO_3$. The assignment to oxyl and bridge radicals derives from spectroscopic signatures unique to their local electronic structure, which for the oxyl radical is its sub-surface vibration[7] and for the bridge radical is an in-plane transition optical dipole. As would be expected of localized charge in O-site radicals and measured specifically by the oxyl's subsurface vibration, the 1.3 ps radicals decay in parallel with the time-resolved photocurrent. Following the initial 1.3 ps formation time, we observe a delay of 4.5 ps and then another 36 ± 10 ps formation time constant. We cannot yet assign a structure to the 36 ps surface species. Decomposition of the white light spectrum for the dominant species (e.g., holes or radicals) at different potentials validates that the radicals arise from valence band holes.

The time constants are unique to the reactive, aqueous interface, independent of potential and surface excitation, and describe two limiting structures (*out-of-plane* and *in-plane*) of O-site radicals. Therefore, they are defined by the vibrational dynamics of water, rather than a surface specific event such as proton coupled electron transfer (PCET). The work thus identifies a formation time related to solvation that is required to stabilize a distribution of both types of O-site radicals; any PCET processes that could differentiate oxyl from bridge radical formation occur faster. Intriguingly, the transfer of energy from the hydroxyl stretch vibration to neighboring water molecules occurs with a 1−1.8 ps time constant in water networks characterized by dilute H-bonds.[16−19] Further, two concomitant time constants of 2 and 4 ps are observed for hydroxyl stretch relaxation within isotopically mixed (HOD in H_2O) water.[19,20] The 4 ps time constant is associated with water equilibrating to an elevated temperature through H-bond breaking. Thereby, we propose the following nonadiabatic kinetic mechanism for stabilizing O-site radicals: The valence band hole has sufficient thermodynamic energy to excite a hydroxyl stretch vibration (0.3 eV) of surface adsorbed or interfacial water. The hydroxyl stretch vibration evolves and transfers energy to reorganize neighboring water molecules (1.3 ps), which creates the solvation environment. Upon the formation of the O-site radicals, a period of H-bond equilibration (~4 ps) ensues.

■ EXPERIMENTAL AND THEORETICAL PROCEDURE

0.08% Nb-doped $SrTiO_3$ by weight (henceforth 0.08% is referred to as 0.1%) $SrTiO_3$ single crystals with crystallographic orientation (100)

DOI: 10.1021/jacs.6b09550
J. Am. Chem. Soc. 2017, 139, 1830−1841

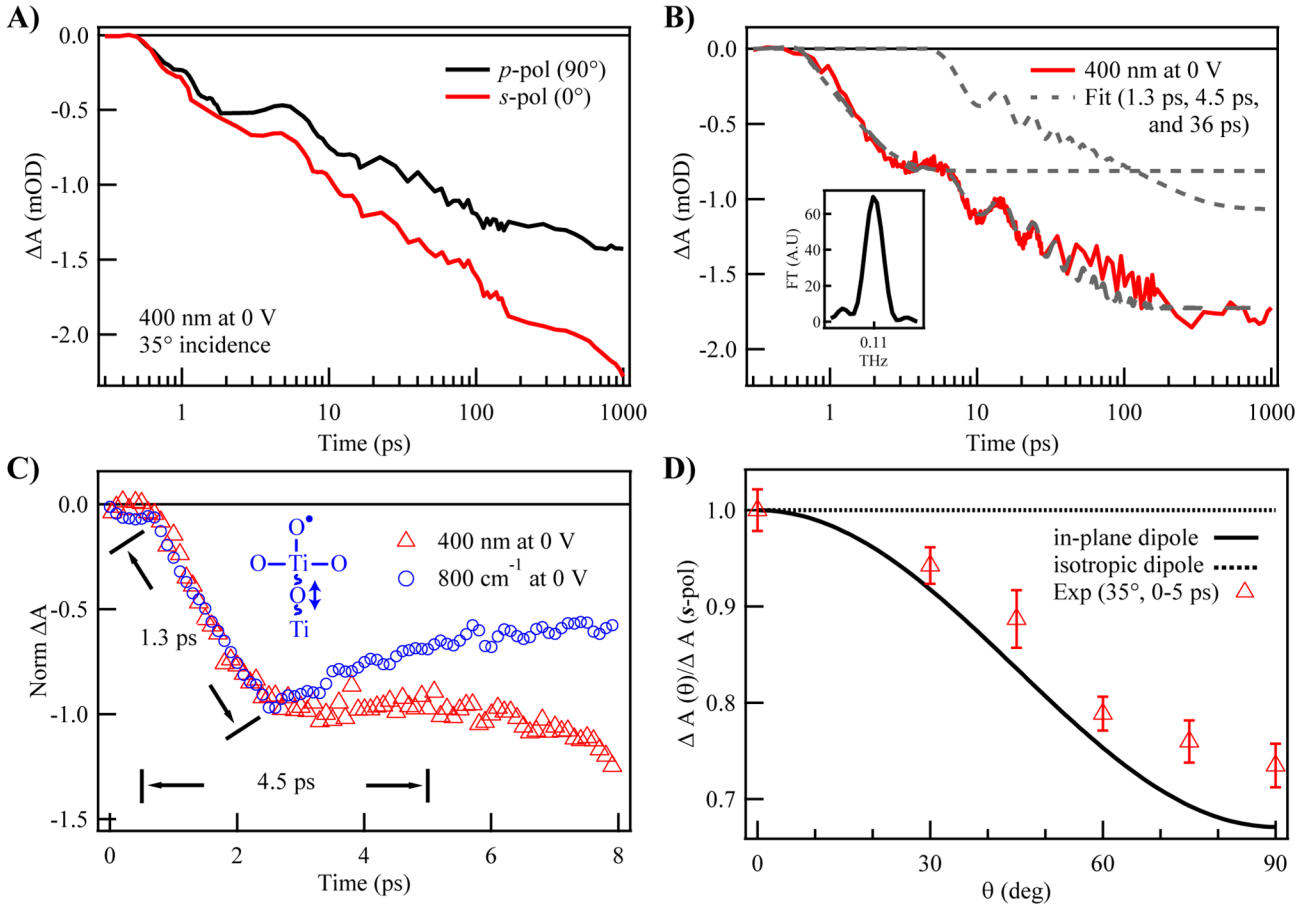

Figure 2. Time-resolved reflectivity after 266 nm light excitation at 0 V probed with 400 nm light. Reported as an emissive absorption change. (A) The trace on the nanosecond time scale for both *s* (red) and *p* (black) polarization, where the ratio of the *s*/*p* absorption change is 0.78. (B) Nanosecond trace with higher time resolution in *s*-polarization (red). The fit, consisting of two independent, rising exponentials, is shown with the two exponential components (1.3 ps, 36 ps) separated (gray, dashed) and added (dark gray, dashed). The fit includes a delay of 4.5 ps between the start points of the two exponentials. The second exponential contains an oscillatory component with a frequency of ∼0.11 THz. The frequency is obtained by a Fourier Transform of the data (inset). (C) The optical (400 nm, red open triangles) and mid-infrared (800 cm^{-1}, blue open circles) traces from 0 to 8 ps; both are taken at 0 V. (D) Polarization dependence of the absorption change reported as ΔA (θ)/Δ*A* (*s*-pol) (red, triangle) and compared to that predicted for transitions with a fully in-plane optical dipole moment (black, solid line) and isotropic dipole moment (black, dashed line). The standard error is calculated from three experimental runs for data between 0 and 5 ps. θ is the polarizer angle, tuned between s-polarization (0°) and *p*-polarization (90°).

were obtained from MTI Corp. (Richmond, CA). The crystals were 0.5 mm thick with polished front sides (Ra < 5 Å) and unpolished backsides. All spectroscopic measurements were performed on the polished front sides. All spectroelectrochemical measurements were performed in a Teflon electrochemical cell with CaF_2 optical windows (3 mm thick). The electrolyte was a 0.1 M aqueous solution of sodium hydroxide for all experiments, unless otherwise noted. The electrolyte was in contact with the atmosphere during measurements. The potential of the n-$SrTiO_3$ photoelectrode with respect to an Ag/AgCl (3 M KCl) reference electrode (MF-2052; Basi, West Lafayette, IN) was controlled by a CHI650E Potentiostat (CH Instruments, Austin, TX). A Pt wire served as the counter electrode. Ohmic contact between the unpolished n-$SrTiO_3$ backside and copper wire was established using Gallium−Indium eutectic (Sigma-Aldrich, St. Louis, MO). For the transient reflectance experiments, an insulating lacquer covered all surfaces except the polished front side of the crystal. The exposed front surface areas of the 0.1% and Nb-doped samples was 25 mm^2.

For the transient experiments, the pump and probe beams were derived from a regeneratively amplified Ti: sapphire laser system (Coherent Legend; Coherent, Inc., Santa Clara, CA) producing pulses with a center wavelength of 800 nm and ≈150 fs temporal width at a 1 kHz repetition rate. Part of the amplifier output was directed into a third harmonic generation setup (Eksma FK-800−200-M, Vilnius, Lithuania) to generate 266 nm light as pump. Another part of the 800 nm beam was frequency doubled to generate 400 nm light as probe. The incident angle of probe on the sample is determined to be 35°, otherwise, the incident angle is somewhat larger. The detailed sample configuration can be seen in Figure 1C and Figure S1A. The polarization of the 400 nm probe beam was controlled by changing the 800 nm polarization using a 1/2-wave plate and a linear polarizer. The pump beam was incident normal to the sample surface. After the sample, the reflected probe beam was focused into an optical fiber, which was coupled to a CCD array spectrometer (CAM-VIS-3; Ultrafast Systems, LLC, Sarasota, FL). In all experiments, the pump beam was modulated by a mechanical chopper (3501; Newport, Inc., Irvine, CA) at a frequency of 500 Hz. The detector output was interfaced with a personal computer, which provided automated control over an optical pump−probe delay stage (MTM250CC1; Newport, Inc., Irvine, CA). The typical incident pump fluence was about 0.05 mJ cm^{-2}, corresponding to carrier densities on the order of 10^{19} cm^{-3}. The excitation beam spot size was 500 μm (fwhm).

The transient infrared measurement procedure was described in detail elsewhere.[7] Briefly, the photoelectrochemical cell includes a diamond attenuated total reflection crystal, Pt counter electrode, and Ag/AgCl reference electrode. The n-$SrTiO_3$ crystal distance to the ATR crystal is controlled by a z-stage. The sample is probed by a single bounce of the evanescent, infrared wave.

DOI: 10.1021/jacs.6b09550
J. Am. Chem. Soc. 2017, 139, 1830−1841

Long-time experiments (up to 500 μs delay) made use of a diode-pumped Q-switched YAG laser (Lightwave Electronics Series 210S, Milpitas, CA) with ~30 ns pulses at 1064 nm as the pump source. The 1064 nm output was converted to 266 nm via fourth harmonic generation using a combination of LBO and BBO crystals. The pump was externally triggered by the amplifier and electronically delayed using a digital delay generator (SRS DG645, Menlo Park, CA).

Density functional theory (DFT) calculations were carried out using the Vienna Ab initio Simulation Package (VASP)[21,22] which employs a planewave basis set and Projected Augmented Wave[23] pseudopotentials. An energy cutoff of 400 eV was used for the planewave expansion in conjunction with pseudopotentials with the following valence electronic configurations Sr: $4s^2 4p^6 5s^2$, Ti: $3p^6 4s^2 3d^2$, O: $2s^2 2p^6$, H: $1s^1$. A 384 atom supercell with cell dimensions of 15.437 Å × 30.0 Å × 15.465 Å including 7 layers of $SrTiO_3$ terminated on either side by water adsorbed TiO_2 layers is used to model the $SrTiO_3$ surface in contact with solvent. Due to the large size of the supercell, the Brillouin zone is sampled only at the zone center. Atoms in supercell images along the nonperiodic y-axis direction are separated by at least 12 Å of vacuum. Structural optimizations were carried out at the DFT +U[24] level employing the Perdew–Burke–Ernzerhof (PBE)[25] functional and an effective Hubbard-U parameter of $U_{O\text{-}2p}$ = 7 eV on the O-2p states. The value of $U_{O\text{-}2p}$ is based on the previous DFT+U analysis by Erhart et al.[26] of hole polaron states in $SrTiO_3$. Structural optimizations of slab geometries were carried out until forces on all the atoms are smaller than 0.02 eV/Å. Furthermore, since the slabs considered exhibit nonzero dipole moments along the nonperiodic direction, self-consistent dipole corrections were applied to the potential, total energy and forces using the approach of Neugebauer et al.[27] Pseudopotentials with small net fractional charges [Sr: 004, Ti: 0.004, O:0.002, H:0.002] are introduced in the spirit of the "pseudo atom" approach of Sinai et al.[28] to mimic hole doping within the system at 0.992 holes per supercell which corresponds to 6.25% hole coverage density at the surface. Solvent effects beyond the first adsorbed water layer were treated using the implicit solvation model due to Mathew et al.[29,30] At the DFT+U optimized geometries, densities of states and optical properties were calculated at the hybrid-DFT level employing the Heyd–Scuseria–Ernzerhof HSE06 screened hybrid functional. Optical transition matrix elements were calculated within the independent particle approximation as implemented in VASP.[31]

RESULTS

Formation Time Constant of Oxyl and Bridge Radicals: 400 nm Probe at 0 V. The perovskite n-$SrTiO_3$ (100)/aqueous interface forms an interfacial electric field that separates photogenerated electron–hole pairs, as depicted in Figure 1A. The water oxidation reaction is initiated by exciting above the band gap (3.25 eV) with a 266 nm (4.66 eV), 500 Hz, 150 fs laser pulse, as shown previously.[13] With this deep UV pulse, a near ideal photon-to-current conversion efficiency (>80%) is achieved with a diode-like photocurrent onset (Figure 1B). Therefore, photoholes generated in the O 2p valence band efficiently migrate to the surface. A number of different O-site radicals could be formed, such as Ti–$O^{\bullet}$ and Ti–$O^{\bullet}$–Ti,[32] and each should correspond to a midgap state within the n-$SrTiO_3$ semiconductor, as depicted in Figure 1A.

In the following section, we use a sub-band gap, 400 nm probe in reflectance and during water oxidation at 0 V to isolate the radicals' optical transitions. In reflectance, the optical penetration depth is 12 nm according to $d = \frac{\lambda}{4\pi n}$ (Figure S1B). For measurements that utilize the polarization properties of the 400 nm probe, the incident angle to the sample is determined to be 35° (Figure 1C, Figure S1A). While s-pol(0°) always refers to a fully in-plane probe polarization, p-pol(90°) contains an out-of-plane component defined by the incident angle. The properties of the reflectance change reported are exclusively associated with the reactive, aqueous interface: they vanish in methanol or deionized water and reduce in pH 7 compared to pH 13 (Figure S2). The time constants are identical for a 0.1% and 0.7% Nb-doped $SrTiO_3$ crystal (Figure S3). The data in the main manuscript are from the 0.1% Nb doped surface at pH = 13. We note that during current evolution, the sample surface changes. Therefore, we confirm the same kinetics on a pristine surface at open circuit. At higher electron energies, the sample postcatalysis still exhibits a LEED pattern of the 1 × 1 surface; a negligibly small amount of metal dissolution results from current evolution (Figure S5 and Figure S6).

Figure 2A shows the kinetic trace of the 400 nm probe at 0 V. We convert the change in reflectance to a change in absorption, according to $\Delta A = -\log(R_{on}/R_{off})$. There are two transitions to consider for hole-related midgap states: the transition of an electron deeper in the valence band to the midgap state, leading to an absorption, and the transition of an electron in the conduction band to the midgap state, leading to stimulated emission. The emissive, charge transfer transition between Ti 3d conduction electrons and the O 2p midgap states should have a much larger cross-section. Indeed, the negative absorption change suggests emission and in this spectral region, emission is expected by $SrTiO_3$ photoluminescence.[14,33] Employing Beer's law and with all the holes generated by the laser pulse reaching the surface at 0 V and 0.05 mJ/cm^2, the cross-section is on the order of a charge-transfer transition, $\sim 10000 \frac{L}{mol - cm}$. We note that since the absorption change relates to the very surface of the sample and the n-$SrTiO_3$ substrate is transparent to 400 nm light (Figure S1B), the limit of a thin absorptive film on a transparent substrate likely applies. Therefore, the reflectance is interpretable in terms of the film's absorptive properties.[34,35]

We observe that the absorption change has a polarized transition optical dipole. Therefore, given the symmetric electronic structure of n-$SrTiO_3$ along x-, y-, z- axes, it relates to a surface species. The absorption change is greater in s-polarization of the 400 nm probe than in p-polarization (Figure 2A for 0 V, Figure S7 for other voltages). The same polarization dependence occurs at open circuit, with a pristine surface (Figure S8). At an incidence angle of 35°, the ratio of p-pol/s-pol is 0.78. Since a fully in-plane optical dipole would lead to a ratio of 0.67 at 35° incidence (Figure S9), this demonstrates a strong in-plane component to the measured absorption change.

Next, the fact that the absorption change increases in time allows us to assign distinct formation times to the surface species. As shown in Figure 2B, the data can be fit with two rising exponentials separated by a delay. The first exponential rise, after convolution with the instrumental response function, has a time constant of 1.25 ± 0.06 ps. The second exponential rise has a time constant of 36 ± 10 ps. A delay in the range of 3–5.5 ps from time 0, when the first rising exponential begins, is required to fit the data with 4.5 ps the best fit. An oscillation, attributable to a 0.11 THz coherent acoustic phonon of $SrTiO_3$,[36] accompanies the second rising exponential (this oscillation is cosine filtered from the data shown in Figure 2A for clarity). The 4.5 ps delay and this oscillation separate the second time constant from the first, such that the fit represents the addition of two species that form independently. The detailed fitting function and procedure can be find in Supporting Information, eq S1.

DOI: 10.1021/jacs.6b09550
J. Am. Chem. Soc. 2017, 139, 1830–1841

We now focus the manuscript on the assignment of the first, 1.3 ps time constant, by using additional spectroscopic signatures of the local electronic structure of the surface species. In other words, we relate the time constant to the population of the surface with particular, stable intermediates. Previously, by ultrafast mid-infrared spectroscopy on the same n-$SrTiO_3$ surface,[7] we identified the oxyl radical (Ti−O•) through a subsurface Ti−O vibration in the plane right below it (Figure 2C inset). As shown in Figure 2C, the rise time of the oxyl's subsurface vibration taken at its peak (800 cm^{-1}) is identical to the 1.3 ps rise of the midgap state. In order to establish this correspondence, both the optical and infrared time traces were taken with 100 fs time steps between 0 and 8 ps under identical reaction conditions of 0.05 mJ/cm^2, 266 nm laser excitation and 0 V applied bias. The rise time between 0 and 2 ps is well within the resolution of our experiment with a Gaussian instrument response time of 200 fs (Figure S10). Two additional experiments confirmed this response time: the faster formation time for surface charge on a different sample (n-GaN) (Figure S11A) and for high light excitations of n-$SrTiO_3$ at open circuit where a bulk carrier component is present (Figure S11B). The rise of the bulk carrier component occurs simultaneously with the light excitation. It is significantly faster than the rise time of the midgap state and therefore defines time zero in Figure 2C; the 0.5 ps delayed onset represents the bulk carrier component that only becomes visible at open circuit (Figure S11B).

These experiments represent a unique achievement in that they map a vibrational signature of a particular radical to an electronic one in time. In interpreting this result, the formation dynamics associated with the vibrational signature are considerably more complex. Multiple physical processes are involved: charge localization to the surface, the development of the radical's vibration, and the coupling of the vibration to neighboring modes. Given its high energy (100 meV), we expect the oxyl's vibration to develop immediately upon the localization of charge to the surface (within 100s fs). However, as demonstrated previously,[7] the subsurface vibration does couple to neighboring modes: to solvent (water librations) and electron (plasmon) excitations. The coupling leads to a distinctive Fano resonance between the discrete vibration and two broad (electron, solvent) continua.[37] The time it takes for the resonance to establish, then, complicates assigning a time constant for populating the surface with oxyl radicals. Further, the width of the vibration (~30 cm^{-1}) leads to a ~1 ps vibrational lifetime, similar to the rise time of the midgap state. While this similarity could be of importance to the kinetic mechanism below or simply coincidental, it does mean that during this time the vibration dephases and populates neighboring modes.

In contrast to the subsurface vibration, the midgap state, by being a purely electronic signature, is insensitive to excitations in the local environment. Therefore, it is exactly through mapping the formation of the midgap state (400 nm) to the rise of the oxyl's vibration (800 cm^{-1}) that we isolate the time constant for populating the surface with oxyl radicals. The evolution of the Fano resonance in time is not limited to this population time. Rather, the Fano resonance evolves over 6 ps, with the major changes concomitant with the sharp drop in the time trace (2−6 ps) (Figure 2C and Figure S12). Interestingly, these major changes in the Fano resonance occur over a ~4 ps time interval that tracks the delay in the midgap state, for which the implications will be discussed below.

Another spectroscopic signature of the local electronic structure of the surface species is the polarized transition optical dipole. In order to characterize the polarization properties more quantitatively, we measured the absorption change between 0 and 5 ps as a function of the probe polarization. At the incident angle of 35°, the 400 nm polarization was tuned from an *s*-polarized (θ = 0°) probe to a *p*-polarized (θ = 90°) probe. In this geometry, the s-polarized (0°) probe is fully *in-plane*, whereas the *p*-polarized (90°) probe is a ratio of *out-of-plane* to *in-plane* components defined by the incident angle. Therefore, Figure 2D reports the absorption change at each angle with respect to the absorption change for the s-polarized (0°) probe: $(\frac{\Delta A(\theta)}{\Delta A(s\text{-pol})})$. For radicals with transitions characterized by totally *in-plane* optical dipole moments, the θ-dependence of the ratio is $\frac{\Delta A(\theta)}{\Delta A(s\text{-pol})} = (\cos(\theta))^2 + (\cos(35°))^2(\sin(\theta))^2$ (solid black line, Figure 2D); no θ-dependence is expected for radicals with transitions characterized by isotropic dipole moments (dotted black line, Figure 2D) and the opposite θ-dependence is expected for radicals with transitions characterized by fully *out-of-plane* dipole moments (Figure S9). The measured ratio largely tracks the *in-plane* predication, which means that a specific type of radical that has a predominant *in-plane* transition optical dipole populates the surface. At large θ that maximizes the *out-of-plane* component, the measured ratio deviates from the fully *in-plane* predication. The assumption of two radical species with similar optical cross sections, but oppositely polarized dipole moments, suggests a ~80/20 ratio of radicals with *in-plane* to *out-of-plane* optical dipole transitions.

Theoretical Calculation of Transition Optical Dipoles of Bridge and Oxyl Radicals. We now turn to the theoretical calculations that assign the *in-plane* optical dipole moment to bridge radical transitions and the *out-of-plane* optical dipole moment to oxyl radical transitions. First-principles density functional theory (DFT) simulations were performed to investigate the light-polarization dependence of emissive transitions between conduction band states and localized midgap hole radical states at the $SrTiO_3$ surface. A 384-atom supercell (Figure 3, Figure S13) consists of a 7-layer $SrTiO_3$ slab terminated on either side by TiO_2 layers and functionalized by water molecules. We find that the lowest energy solvent configuration at the surface involves a partial dissociation of adsorbed water molecules so that 50% of the Ti sites are H_2O adsorbed, while the rest are OH^- adsorbed and the dissociated protons attach to nearby surface O sites. The top TiO_2 layer of all the slabs considered is modeled with this partially dissociated water configuration. Intact water molecules functionalize the bottom TiO_2 layer of the slabs, which renders it inactivate to hole doping relative to the top layer. The geometry of the bottom TiO_2 layer and adsorbed water is held fixed across all the hole-doped configurations considered. We model five different O-2p hole-radical configurations where the hole is localized either in the central bulk region of the slab or at the surface where it can form oxyl (Ti−O•) or bridge (Ti−O•−Ti) radicals (Figure S13). Among these, we find the bridge (Ti−O•−Ti) radical configuration with a O-$2p_y$ hole to be the lowest in energy separated by ~0.1 eV from the nearest oxyl (Ti−O•) radical configuration. Interestingly, the magnitude of the (Ti−O•−Ti) and (Ti−O•) energy difference is smaller but is opposite in sign to that predicted at the rutile TiO_2 surface where the geometry and water adsorption characteristics are

DOI: 10.1021/jacs.6b09550
J. Am. Chem. Soc. 2017, 139, 1830−1841

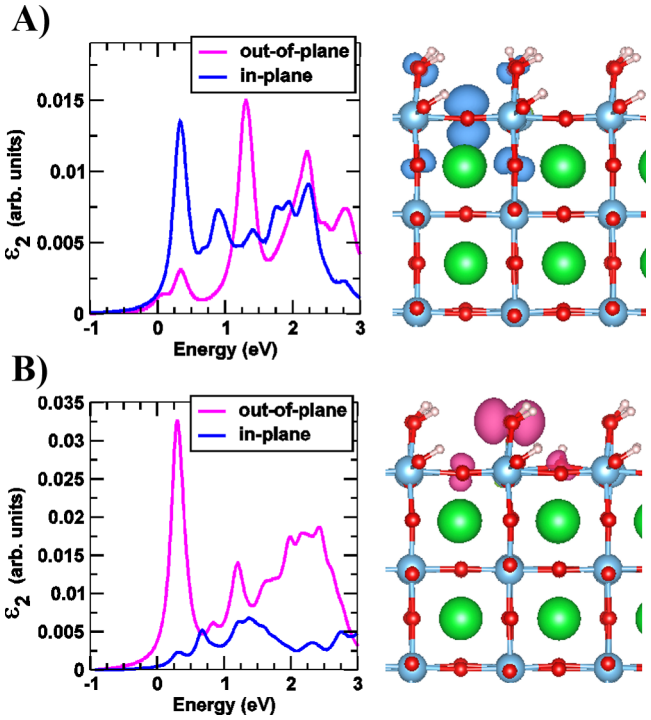

Figure 3. Theoretical calculation of optical transition dipole strengths. (A) (left) Intensity and polarization dependence of optical transitions between the midgap bridge (Ti−O•−Ti) surface hole radical and the conduction band of $SrTiO_3$. Since absolute transition energies are not calculated, for clarity, the energy of the transition to the lowest conduction band state is referenced to 0.0 eV. (right) Spin density isosurface (purple) for the localized bridge surface radical is shown. (B) (left) Intensity and polarization dependence of optical transitions between the midgap surface oxyl (Ti−O•) hole state and the conduction band of $SrTiO_3$. For clarity, the energy of the transition to the lowest conduction band state is referenced to 0 eV. (right) Spin density isosurface (deep-blue) for the localized oxyl surface radical is shown.

different. Within the theoretical framework employed in this work, the configurational energies of the surface radicals can be calculated relative to the O-2p hole localized in the bulk region of the slab (Figure S13). By referencing this bulk-localized hole configuration to the self-trapped hole configuration in bulk $SrTiO_3$ from previous calculations by Janotti et al.,[38] we assume a self-trapping energy of the bulk hole polaron to be ∼0.05 eV. Relative energy differences between this bulk-localized configuration and oxyl or bridge surface-localized configurations calculated in the current work (Table S1) then indicate that the surface-localized configurations have self-trapping energies in the range of 0.19−043 eV. Therefore, optically excited valence band hole carriers can transform into either bridge or oxyl radicals at the surface by transferring energy to vibrational degrees of freedom during the relaxation process. Density of states plots in (Figure S14) indicate all radicals lead to localized mid gap hole states that are optically active with respect to emissive transitions from free-carrier like conduction-band states that are populated either by n-doping or photoexcitation. Accordingly, the contribution to the imaginary part of the dielectric matrix (ε_2) obtained by restricting the allowed transitions to those between the midgap hole states and the conduction band manifold was calculated which provides a qualitatively accurate description of the nature of the emissive transitions probed in the experiment. The calculated diagonal components of ε_2 were separated into *in-plane* and *out-of-plane* components of light-polarization and are shown in Figure 3 for the two lowest energy configurations; all other configurations are shown in Figure S13. Assessments of *in-plane* and *out-of-plane* character are independent of surface excitation (Figure S14). We find that optical transitions involving the bridge (Ti−O•−Ti) radical state and states near the conduction band minimum are principally *in-plane*-polarized (Figure 3A) and this character of the optical transitions also extends up to 1 eV higher into the conduction band. Given that the exciton binding energy in $SrTiO_3$ is ∼0.22 eV,[39] we expect the *in-plane* polarization in the case of the bridge (Ti−O•−Ti) radical to be a feature that is robust with respect to the independent particle approximation employed for the calculation of the optical transitions. In contrast, optical transitions involving the oxyl (Ti−O•) radical state and low-lying conduction band states are largely of *out-of-plane*-polarized character and transitions from states ∼0.75 eV higher are of mixed character. Bulk-localized hole states on the other hand are not expected to produce a polarization-dependent signal as the *x*-, *y*- and *z*- directions are equivalent within the bulk of the material.

Radical Distribution and Surface-Limited Reaction Kinetics: Voltage Dependence with 400 nm Probe. We turn to further experiments with the 400 nm probe, but now under different applied voltages. The experiments described complete the picture of a single time constant of a surface-limited reaction producing a distribution of both bridge and oxyl radicals. First, we address a disparate voltage dependence of the bridge and oxyl radical populations. Figure 4A shows time traces of the maximum absorption change for the oxyl's subsurface vibration at open circuit and 0 V (800 cm^{-1}), compared to that of the radicals' midgap state at open circuit and 0 V (400 nm). The infrared and optical data at 0 V are normalized to each other, while the open circuit data are denoted by a scale factor with respect to this normalization. For the 400 nm trace at open circuit, there is an additional offset due to the bulk carrier contribution. While the oxyl's population, measured by its specific vibration, is smaller at 0 V (×0.36) than at open circuit, the radicals' population, measured by the midgap state, is much larger (×9.5). Throughout, the 1.3 ps formation time constant is preserved. The disparate voltage dependence implies that, while oxyl and bridge radicals are both created and with the same time constant, the bridge radicals preferentially populate the surface at oxidative potentials. This is also suggested by the 80/20 ratio derived from the polarized transition optical dipole (Figure 2D). For oxyl and bridge radicals to populate the O-sites indiscriminately, the anticipated ratio of bridge to oxyl radicals on the (100) surface of $SrTiO_3$ would be 67/33.

To show that the surface thus populated is involved in bond formation, Figure 4B compares a spectroscopic probe of the surface to the time-resolved photocurrent. Here, the spectroscopic probe chosen is the oxyl's subsurface vibration, rather than the midgap state. Since the vibration is very specific to charge localized into a titanium oxyl, its decay in principle counts charge leaving the surface while avoiding dynamics associated with later intermediates of the cycle. Indeed, the decay of the oxyl's subsurface vibration parallels the decay of the photocurrent between 5 and 400 μs. The fact that a single type of O-site radical decays with the same time constant as the overall charge leaving the surface implies that the initial radical distribution created by the 1.3 ps time constant and consisting

DOI: 10.1021/jacs.6b09550
J. Am. Chem. Soc. 2017, 139, 1830−1841

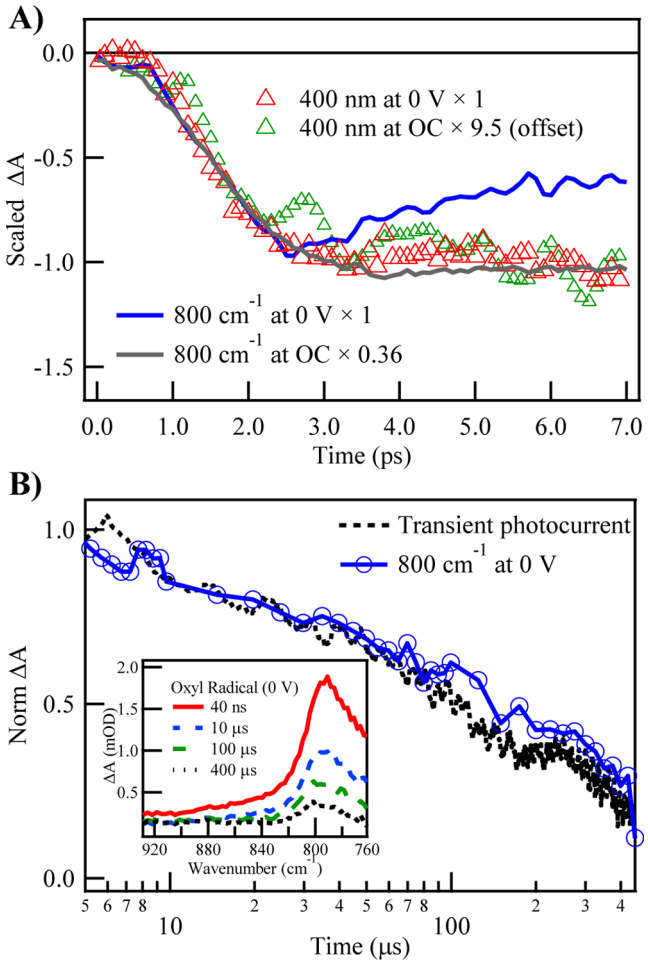

Figure 4. Formation (0–7.5 ps, A) and decay (5–450 μs, B) of radicals under applied voltage. (A) Midgap state (400 nm) at 0 V (red, open triangle) and open circuit (green, open triangle) compared to the oxyl's subsurface vibration (800 cm^{-1}) at 0 V (blue, solid line) and at open circuit (gray, solid line). The scale factors of the open circuit traces are noted with respect to the 0 V traces. The 0 V traces (400 nm and 800 cm^{-1}) are normalized to eachother. (B) Time-resolved photocurrent at 0 V (black, dashed line) compared to the decay of the oxyl's subsurface vibration (800 cm^{-1}) at 0 V (blue line, open circle). The inset of (B) shows the spectrum of the subsurface vibration at 40 ns (red, solid), 10 μs (blue, dashed), 100 μs (green, dashed) and 400 μs (black, dashed).

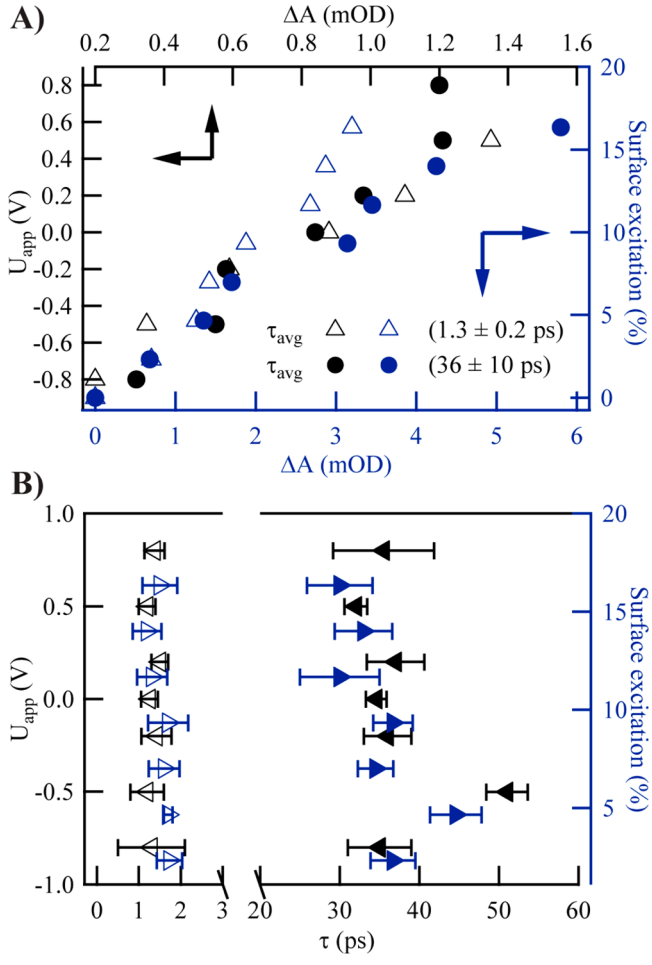

Figure 5. Radical population probed at 400 nm under applied voltage. (A) Amplitudes obtained for the two component fit of Figure 2B with applied voltage from −0.8 V to +0.8 V (left, top, black dots and open black triangles) and 0–20% surface excitation at 0 V (right, bottom, blue dots and open blue triangles). (B) Time constants for the two component fit with applied voltage from −0.8 V to +0.8 V at 2.3% surface excitation (left, black triangles) and at 0 V with 0–20% surface excitation (right, blue triangles). The reported time constants (1.3 ps, 36 ps) and their error (±0.2 ps, ± 10 ps) come from an average of all the data points shown.

of diverse O-site radicals (Figure 4A) concertedly decays to form chemical bonds (Figure 4B).

Finally, the voltage independence of the formation time constants demonstrates explicitly a single, surface-limited reaction of $[h^+] + [S] \rightarrow [R]$, where [S], [R], and $[h^+]$ denote respectively the concentration of surface active sites, radicals, and valence band holes. As shown in Figure 5, the applied voltage and light excitation modulate the reactant $[h^+]$ and product [R] concentrations. The light excitation is reported as a % surface excitation of all available surface O sites, where all the photoholes generate radicals. At higher oxidative potentials (greater than −0.8 V, Figure 1B), the radicals' absorption change increases (Figure 5A) while the time constants (1.3 ps, 36 ps) are not altered (Figure 5B, Figure S15A). With increasing surface excitation at 0 V, the radicals' absorption change also increases (Figure 5A) while the time constants are not altered (Figure 5B, Figure S15B). The fact that increasing the product concentration does not modify the time constants demonstrates a surface limited, zero-order reaction. Further, at open circuit, the radical concentration saturates with excitation (Figure S16) at ∼4–5%.

While the reaction is surface limited, the product concentration increases with both oxidative potential and surface excitation. The surface excitation concomitantly increases the anodic current (Figure S16). Hence, both potential and current modify the surface active site concentration, [S]. Specifically for surface sites associated with localized holes, the observed linear increase (Figure 5A) with oxidative potential and anodic current is expected.

A rate model of the reaction $[h^+] + [S] \rightarrow [R]$ summarizes the dynamics. The rate equations for [R] and [S] are

$$\frac{d[R]}{dt} = k[h^+]^x[S]^y \quad (1)$$

and

DOI: 10.1021/jacs.6b09550
J. Am. Chem. Soc. 2017, 139, 1830–1841

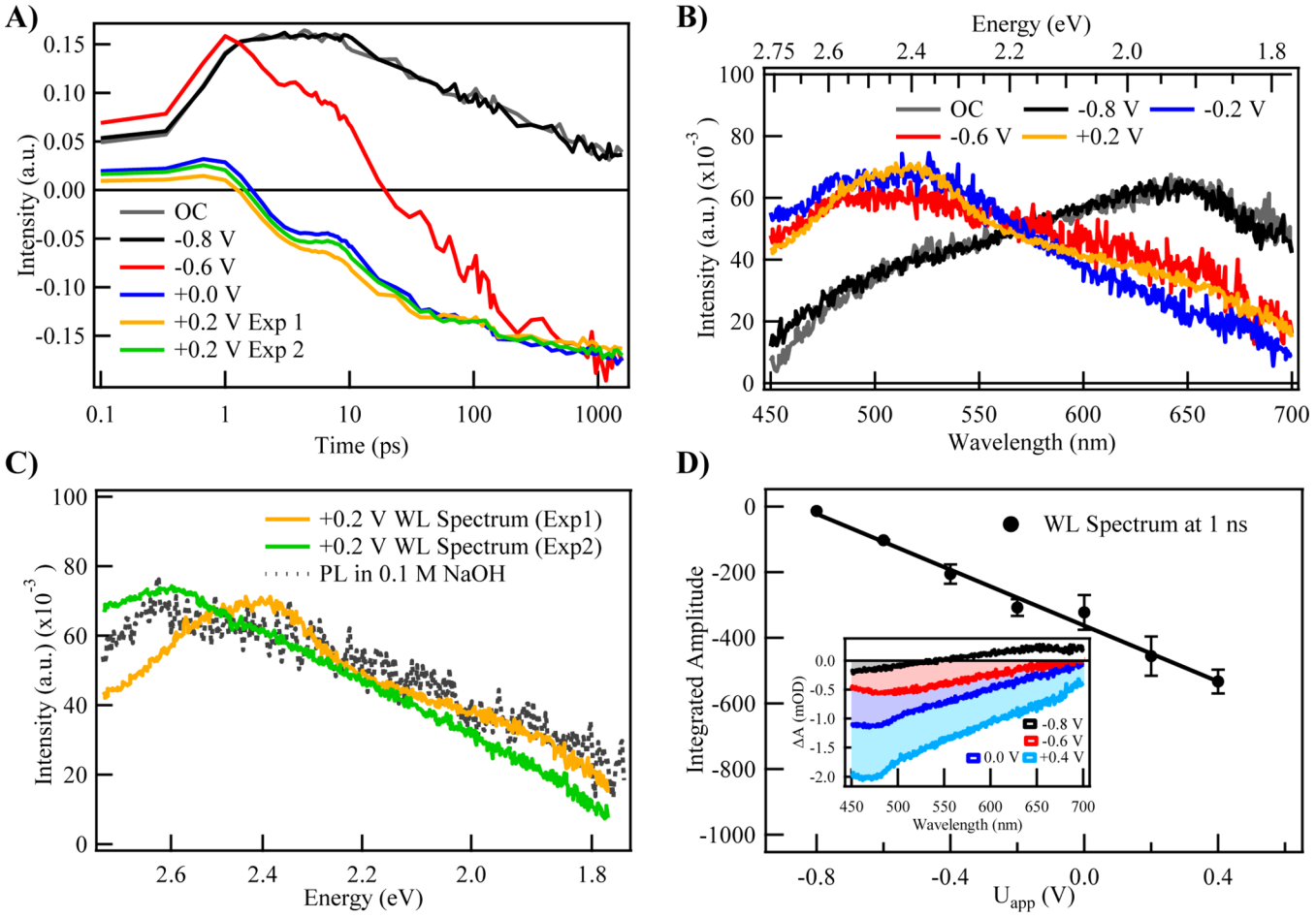

Figure 6. Broad-band white light probe of both radicals and valence band holes. From the singular value decomposition analysis, (A) the eigenkinetics and (B) eigenspectra of the first principal component at select voltages and (C) eigenspectra at +0.2 V (two trials, Exp1 and Exp2) compared to photoluminescence spectra of 0.1% Nb doped SrTiO3 in 0.1 M NaOH. (D) Integrated amplitude of the emission at 1 ns after pump excitation for −0.8 V to +0.4 V. Error bars represent the standard deviation between two measurements at each voltage. The inset of (D) shows the raw, noise-reduced traces at 1 ns at select voltages.

$$\frac{d[S]}{dt} = -k[h^+]^x[S]^y \quad (2)$$

where k is the equilibrium rate constant. A zero order, surface limited reaction is given by $x = 0$ and $y = 1$, which is also consistent with a one hole transfer reaction (x and y are both ≤ 1). Solving eqs 1 and 2 leads to $[R]_t = [S]_0 (1 - e^{-kt})$, where $[S]_0$ is the concentration at which the surface saturates with radicals (tuned by the reaction conditions) and at the potentials investigated, k is constant. This reaction models the observed kinetics because the formation dynamics can indeed be fit with rising exponentials, the radical concentration increases with the available surface sites (e.g., $[S]_0$), and the rate constants are independent of potential. Finally, the 1.3 ps time constant derived from this rate model is especially preserved under a wide range of experimental conditions, with an average deviation of ±0.2 ps (Figure 5B).

Charge Transfer Kinetics of Radicals and VB Holes: Decomposition of White Light Probe with Applied Voltage. In the last results section, we turn to experiments that finish the description of the full charge-transfer reaction required to create one-electron intermediates. Namely, the formation of the O-site radicals is observed to arise from the concomitant decay of valence band holes. A broad-band white light probe of the n-$SrTiO_3$ surface with applied voltage, together with singular value decomposition (SVD), is employed. Figure 6A and 6B show, as a function of applied voltage, the first principal component of the kinetics and their associated spectra, respectively. This analysis also defines the spectrum of the oxyl and bridge radicals' optical emission.

At voltages greater than 0 V, the absorption change is almost entirely emissive and the dynamics, containing two formation times with a delay in-between, are identical to the 400 nm probe (Figure S17). The spectrum of the radicals at 0 V and beyond peaks at 2.6 eV (475 nm), but is spectrally very broad (400−600 nm). The radicals' decomposed spectrum is identical to the photoluminescence spectrum from $SrTiO_3$ (Figure 6C), which had previously been associated with various proposed midgap states.[38,40] The photoluminescence shown in Figure 6C is specifically from a sample dipped in pH 13 water, which significantly enhances the photoluminescence compared to air (Figure S18). Importantly, the measured, decomposed spectrum can differ between samples, shifting by ∼0.2 eV (Figure 6C) while the formation dynamics are not altered (Figure 6A). This suggests that diverse radical species encompassed by the emission form in ratios sensitively subject to reaction conditions. Furthermore, through the SVD analysis, we can assign the 1.3, 4.5, and 36 ps formation dynamics to the entire emission spectrum.

DOI: 10.1021/jacs.6b09550
J. Am. Chem. Soc. 2017, 139, 1830−1841

At more reductive potentials, there is an additional, positive absorption change with its own kinetic component. At open circuit or equivalently, −0.8 V, the absorption change is entirely positive and displays a ∼150 ps exponential decay. The transient spectrum associated with the positive absorption change at −0.8 V peaks at 1.9 eV (650 nm). Unlike the radicals' absorption change that saturates with surface excitation at open circuit (Figure S16), this red-shifted absorption change only increases with fluence (Figure S19A and Figure S19B). Further, it is not affected by methanol or pH (Figure S19C and Figure S19D). Taken together, the significant red-shift of the spectrum, the lack of a surface saturation, and no spectral or kinetic change with different electrolytes, the spectral component isolated at −0.8 V is naturally assigned to bulk holes in the valence band. The overlap of this transient spectrum with that of the radicals' spectrum explains why only at shorter wavelengths, near 400 nm, are the formation dynamics of the radicals isolated across a broad voltage range, including at open circuit. It also explains the bulk hole component observed at open circuit with a 400 nm probe and used to identify time zero.

Clearly, the potential-dependent white light spectra identify the dynamics of two distinctly different species: at oxidative potentials, the formation of oxyl and bridge radicals, and at reductive potentials, the decay of valence band holes. Similar to that observed with a 400 nm probe, the radical population increases linearly with oxidative potential (Figure 6D). Since the formation time constants are not altered by the potential (Figure 6A 0 V and +0.2 V), but the radicals' population increases, the valence band hole decay should be potential-dependent: in order to fill more surface sites with radicals within the same time frame, the hole population has to deplete faster. Such a potential dependence was observed previously[13] and a detailed model that includes the potential dependent decay of holes $k(V)$ and the potential independent formation dynamics of the radicals will be considered in a separate publication. We note that the potential dependence should result from a change in the free energy difference across the interface. Indeed, the applied voltage can drop across the screening, Helmholtz layer at the interface and move the valence band down in energy,[13,41−44] lowering the potential of the valence band holes.

DISCUSSION

In this manuscript, we focused on assigning the 1.3 ps formation time constant of the midgap state to particular one-electron intermediates of photocatalytic water oxidation at the n-$SrTiO_3$/aqueous interface. The 1.3 ps time constant and the 4.5 ps delay that follows it are separately attributed to titanium oxyl and bridge radicals by (1) an identical population time for oxyl radicals, as measured by its subsurface vibration at 800 cm^{-1}; (2) a predominantly *in-plane* optical dipole moment ascribed specifically to bridge radicals (Ti−O$^{\bullet}$−Ti).

The fact that the two limiting structures of single O-site radicals—oxyl (*out-of-plane*) and bridge (*in-plane*)—both populate the surface with the 1.3 ps time constant is given by (1) a detailed polarization dependence that shows the measured dipole moment to include an *out-of-plane* component; (2) a disparate potential dependence of the bridge (via the midgap state) and oxyl (via the subsurface vibration) populations, while the 1.3 ps time constant is potential independent; (3) an assignment of the 1.3 ps time constant and the 4.5 ps delay that follows it to the entirety of the broad emission spectrum, which can shift depending on the radical distribution (∼0.2 eV).

We now turn to the physical process that defines the 1.3 ps time constant and the 4.5 delay that follows it. Most generally, localizing a valence band hole to a water adsorbed surface site involves hole transport across the depletion region of the semiconductor, molecularly specific surface events such PCET, and the solvation dynamics of water. However, since the time constants are surface-limited, they should be independent of the hole location within the depletion region. Further, applied voltages, which significantly modify the electric field across the depletion region (from 7×10^5 V/cm at −0.6 V to 1.4×10^6 V/cm at 0 V), do not alter the time constants.

The fact that the dynamics are exclusively associated with the reactive, aqueous interface, not altered by potential and surface excitation, and describe populating the surface with two limiting structures of O-site radicals (*in-plane* and *out-of-plane*), suggests that they are not controlled by PCET, but are rather defined by the solvation dynamics of water. We first discuss the 1.3 ps time constant in this context. Importantly, a similar time constant appears in mid-infrared pump−probe spectroscopy of bulk and interfacial water, where the hydroxyl stretch vibration (0−1) is excited and its relaxation probed over a broad frequency range. The hydroxyl stretch transfers its energy to lower energy excitations of neighboring water molecules, which include bending and librational modes, as well as the collective H-bond network.[16−20,45−47] In most studies, HOD within either H_2O or D_2O probes the relevant dynamics. The time constant reported spans between 0.7 and 1 ps for OH within D_2O[18,19,46] and 1.4−1.8 ps for OD within H_2O.[18−20,47,48] Though more challenging to determine, a faster relaxation time of 200−300 fs was suggested for OH stretches within bulk H_2O.[16,49] At interfaces, sum frequency generation investigates adsorbed OH: a time constant of 1.3 ps is found at a hydrophobic silica surface[16] and a probe frequency-dependent time constant of 0.5−1.3 ps is found at the hydrophilic silica surface.[50] A 1.3 ps time constant is also found for hydroxyl stretch relaxation of water molecules surrounded by acetone in CCl_4.[17]

The longer (>1 ps) time constant observed for radical formation suggests the relevance of a dilute H-bond network. In the systems quoted above, the ones that represent a dilute H-bond network with a 1−1.8 ps time constant are (1) Isotopically dilute water networks (e.g., HOD in H_2O)[18,19] (2) A H-bond network for mixed water: acetone: CCl_4 where it is suggested that one hydrogen interacts with acetone at a time[17] and (3) Adsorbed OH at hydrophilic (0.5−1.3 ps)[50] and hydrophobic (1.3 ps) surfaces.[16]

The lack of an effect of deuteration on the kinetics supports a dilute H-bond network limit. As observed for the vibrational relaxation of the hydroxyl stretch in water: acetone: CCl4 mixtures, the radicals' formation time lacks an H/D exchange (Figure S20). Further, the coupling constant defining the Fano resonance between the oxyl's subsurface vibration and librations is not sensitive to deuteration, despite deuteration significantly modifying the density of librations near the vibration. This is reflected in the relatively constant width of the Fano resonance (30−45 cm^{-1} or 3−4 meV).[7]

By connecting the vibrational dynamics of the hydroxyl stretch to the formation of surface radicals, a kinetic mechanism emerges to describe how a delocalized valence band hole generates an O-site radical. As noted earlier in the theory section, the surface-localized radicals are characterized by energies ∼0.19−0.43 eV lower than a valence band hole.

DOI: 10.1021/jacs.6b09550
J. Am. Chem. Soc. 2017, 139, 1830−1841

Therefore, as the initially photoexcited Valence Band Maxiumum (VBM) holes relax first into subsurface hole-polarons and subsequently into surface-localized bridge or oxyl radicals, they are expected to transfer the excess energy into the nearby solvent vibrational degrees of freedom. In particular, it emerges clearly from the theoretical modeling that assuming a 50% admixture of adsorbed H_2O and OH^- species, creating any of the stable surface-localized radical configurations requires the breaking of one OH bond. The nonadiabatic transfer of some of the VBM hole excess energy into a hydroxyl stretch could facilitate this process by reorganizing water molecules near the host O-2p hole site. We further note that starting from a subsurface localized hole, the nonadiabatic relaxation process into bridge and oxyl radicals could proceed via similar transition states involving a stretched O−H−O configuration wherein an oxygen site in the top TiO_2 layer exchanges a proton with a Ti adsorbed oxygen with the direction of the exchange determining the final product. Alternatively, a Ti adsorbed H_2O and Ti adsorbed OH^- group could exchange a proton to facilitate the stabilization of a surface radical. Such a mechanism is schematically diagrammed in Figure 7: The photohole in the solid-state band loses some of its energy to excite a hydroxyl stretch either as a 0−1 vibration in nearby water or on a surface-adsorbed species. As the hydroxyl stretch evolves and transfers energy to neighboring water molecules, the solvation environment engenders the transition state needed for radical formation. The solvation environment created by such a high energy, nonadiabatic mechanism is expected to yield diverse oxygen radicals likely through similar transition states that are not unique to a particular molecular structure, e.g., bridge or oxyl. Assuming the initial descent toward the transition state is rapid compared to the dynamics associated with the hydroxyl stretch relaxation, the latter, with a 1.3 ps time constant would be the rate-determining factor for all radicals. We note that molecular dynamics simulations[51] that start on the ground state potential energy surface and depend on thermal fluctuations to access the transition states do not describe this mechanism. More extensively, nonadiabatic molecular dynamics simulations[52] will be necessary to model the dynamics of the relaxation process that converts VBM delocalized holes into surface-localized radicals.

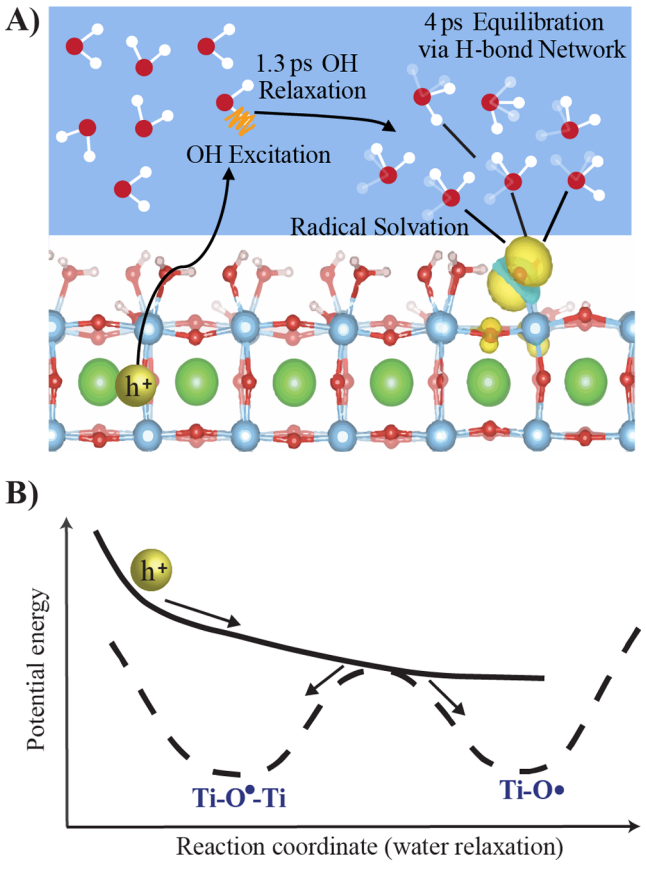

Figure 7. Diagram of nonadiabatic kinetic mechanism. (A) By exciting a hydroxyl stretch vibration that transfers energy to neighboring water molecules, a photohole engenders the solvation environment necessary for radical formation. The 1.3 ps vibrational relaxation is followed by a ∼4 ps period of H-bond equilibration. (B) Proposed reaction diagram of forming oxyl (Ti−O•) and bridge (Ti−O•−Ti) radicals from energetic valence band holes.

The thermodynamics required for this kinetic mechanism matches that expected. While the exact energetic position of the oxyl and bridge radicals within the gap may not be known yet precisely, theory suggests they are approximately ∼0.4 eV away from the valence band. Further, a ∼0.3−0.4 eV potential energy difference to the O_2/H_2O Nernstian potential is common for photocatalytic water oxidation on a number of transition metal oxides, as evidenced by catalysis initiated using the $Ru(bpy)_3$ dye.[53] Such a potential energy difference is the minimum necessary to excite the hydroxyl stretch vibration.

We now turn to the sequential nature of the 1.3 ps time constant and the 4.5 ps delay. Following the relaxation of the hydroxyl stretch intermolecularly, water forms an elevated temperature equilibrium. A number of studies[16,20,49] find that the equilibration occurs after the hydroxyl stretch relaxes and primarily by the breaking of H-bonds. For the dilute H-bond network of the OD stretch in H_2O, the time scale to reach the elevated temperature equilibrium is 4 ps.[19,20] This ∼4 ps time scale is seen to follow the 1.3 ps time constant for both the midgap state and the oxyl's subsurface vibration. In the latter, it appears as a 2−6 ps interval during which the Fano resonance evolves. Intriguingly, this suggests that we are sensitive to the H-bond breaking events involved in the equilibration process through the 4.5 ps delay and the time evolution of the vibration's coupling to librations. Future work will utilize ultrafast broad band mid-infrared light to directly probe the response of water molecules to the creation of oxyl and bridge radicals.

All of these dynamics concern the conversion of a hole into a radical that localizes the positive charge. However, in order to form the radical, this hole had to separate from the initially excited valence band population. Using the broad-band white light probe and SVD analysis, we were able to separately identify the formation dynamics of radicals and the decay of the valence band hole population. We demonstrated that reaction conditions, tuned by potential and surface excitation, modify the number of surface active sites. Future studies will explore this connection between the number of active sites, reaction conditions, and the solvation dynamics of water that stabilize the radicals.

■ CONCLUSIONS

The results report on the time constant (1.3 ps) by which oxyl (Ti−O•) and bridge (Ti−O•−Ti) radicals arise from valence band holes at the n-$SrTiO_3$/aqueous interface during photocatalytic water oxidation. The fact that the time constant is exclusively associated with the reactive, aqueous interface, is not

DOI: 10.1021/jacs.6b09550
J. Am. Chem. Soc. 2017, 139, 1830−1841

altered by potential and surface excitation, and describes populating the surface with two limiting structures of O-site radicals (*in-plane* and *out-of-plane*) led to a proposed, nonadiabatic mechanism for forming stable one-electron reaction intermediates based on their solvation at aqueous interfaces.

■ ASSOCIATED CONTENT

Supporting Information

The Supporting Information is available free of charge on the ACS Publications website at DOI: 10.1021/jacs.6b09550.

Experimental probe geometry and sample reflectivity. Transient kinetics of 0.1% Nb-doped $SrTiO_3$ in methanol, Deionized H_2O and 0.1 M NaOH at open circuit Transient kinetics of 0.1% and 0.7% Nb-doped $SrTiO_3$ in 0.1 M NaOH at +0.4 V applied potential. SEM image, ICP and LEED analysis of sample roughening. Magnitude of photoinduced change at different applied potential and polarization. Early time kinetics with polarizer angle. Instrumental response function of Ti:sapphire laser. Early time kinetics traces for 0.1% Nb-doped $SrTiO_3$ compared with *n*-GaN. Spectra evolution with time for 0.1% Nb-doped $SrTiO_3$ in mid-infrared wavelength range at 0 V applied potential. Atomistic supercell model and electronic density of states. Bridge and oxyl hole transition dipole polarization. Transient kinetics of 0.1% Nb-doped $SrTiO_3$ from −0.8 V to +0.5 V applied potential and 2 to 14% surface excitation. Radical population with reaction current. Transient kinetics for SVD spectrum compared with 400 nm. Photoluminescence spectra in 0.1 M NaOH and in air. White light continuum spectra of 0.1% Nb-doped $SrTiO_3$ from 450 to 700 nm at different excitation fluence. Transient kinetics of 0.1% Nb-doped $SrTiO_3$ in 0.1 M NaOH and NaOD. Fitting procedure. (PDF)

■ AUTHOR INFORMATION

Corresponding Author

*tanjacuk@berkeley.edu

ORCID

Xihan Chen: 0000-0001-7907-2549

Tanja Cuk: 0000-0002-1635-2946

Notes

The authors declare no competing financial interest.

■ ACKNOWLEDGMENTS

This material is based upon work supported by the Department of Energy Office of Basic Energy Sciences, under the CPIMS program KC030102 (FWP no. CH12CUK1). We thank Dr. Dylan Lu for help with taking the photoluminescence measurements and Professor Peidong Yang for the use of the photoluminescence instrument. We would also like to thank Dr. Miquel Salmeron and Dr. Heinz Frei for proof-reading the manuscript and offering very helpful suggestions. Density functional theory simulations were performed as part of a User Project with C.D.P. and D.P. at The Molecular Foundry (TMF), Lawrence Berkeley National Laboratory, and calculations were executed on their Vulcan and Nano compute clusters, administered by the High-Performance Computing Services Group at LBNL. TMF is supported by the Office of Science, Office of Basic Energy Sciences, of the U.S. Department of Energy, under Contract No. DE-AC02-05CH11231.

■ REFERENCES

(1) Licht, S.; Wang, B.; Mukerji, S.; Soga, T.; Umeno, M.; Tributsch, H. *J. Phys. Chem. B* **2000**, *104*, 8920−8924.
(2) Eisenberg, R.; Gray, H. B. *Inorg. Chem.* **2008**, *47*, 1697−1699.
(3) Siegbahn, P. E. M. *Inorg. Chem.* **2008**, *47*, 1779−1786.
(4) Klahr, B.; Hamann, T. *J. Phys. Chem. C* **2014**, *118*, 10393.
(5) García-Mota, M.; Vojvodic, A.; Abild-Pedersen, F.; Nørskov, J. K. *J. Phys. Chem. C* **2013**, *117*, 460−465.
(6) García-Mota, M.; Vojvodic, A.; Metiu, H.; Man, I. C.; Su, H.; Rossmeisl, J.; Nørskov, J. K. *ChemCatChem* **2011**, *3*, 1607−1611.
(7) Herlihy, D. M.; Waegele, M. M.; Chen, X.; Pemmaraju, C. D.; Prendergast, D.; Cuk, T. *Nat. Chem.* **2016**, *8*, 549−555.
(8) Zandi, O.; Hamann, T. W. *Nat. Chem.* **2016**, *8*, 778−783.
(9) Zhang, M.; de Respinis, M.; Frei, H. *Nat. Chem.* **2014**, *6*, 362−367.
(10) Le Formal, F.; Pastor, E.; Tilley, S. D.; Mesa, C. A.; Pendlebury, S. R.; Gratzel, M.; Durrant, J. R. *J. Am. Chem. Soc.* **2015**, *137*, 6629−6637.
(11) Barroso, M.; Pendlebury, S. R.; Cowan, A. J.; Durrant, J. R. *Chem. Sci.* **2013**, *4*, 2724−2734.
(12) Pendlebury, S. R.; Wang, X.; Le Formal, F.; Cornuz, M.; Kafizas, A.; Tilley, S. D.; Gratzel, M.; Durrant, J. R. *J. Am. Chem. Soc.* **2014**, *136*, 9854−9857.
(13) Waegele, M. M.; Chen, X.; Herlihy, D. M.; Cuk, T. *J. Am. Chem. Soc.* **2014**, *136*, 10632−10639.
(14) Yamada, Y.; Yasuda, H.; Tayagaki, T.; Kanemitsu, Y. *Appl. Phys. Lett.* **2009**, *95*, 121112.
(15) Yamada, Y.; Sato, H. K.; Hikita, Y.; Hwang, H. Y.; Kanemitsu, Y. *Phys. Rev. Lett.* **2013**, *111*, 047403.
(16) McGuire, J. A.; Shen, Y. R. *Science* **2006**, *313*, 1945−1948.
(17) Gilijamse, J. J.; Lock, A. J.; Bakker, H. J. *Proc. Natl. Acad. Sci. U. S. A.* **2005**, *102*, 3202−3207.
(18) Laenen, R.; Simeonidis, K.; Laubereau, A. *J. Phys. Chem. B* **2002**, *106*, 408−417.
(19) Kropman, M. F.; Nienhuys, H.; Woutersen, S.; Bakker, H. J. *J. Phys. Chem. A* **2001**, *105*, 4622−4626.
(20) Steinel, T.; Asbury, J. B.; Zheng, J.; Fayer, M. D. *J. Phys. Chem. A* **2004**, *108*, 10957−10964.
(21) Kresse, G.; Furthmüller, J. *Comput. Mater. Sci.* **1996**, *6*, 15−50.
(22) Kresse, G.; Furthmüller, J. *Phys. Rev. B: Condens. Matter Mater. Phys.* **1996**, *54*, 11169−11186.
(23) Blöchl, P. E. *Phys. Rev. B: Condens. Matter Mater. Phys.* **1994**, *50*, 17953−17979.
(24) Dudarev, S. L.; Botton, G. A.; Savrasov, S. Y.; Humphreys, C. J.; Sutton, A. P. *Phys. Rev. B: Condens. Matter Mater. Phys.* **1998**, *57*, 1505−1509.
(25) Perdew, J. P.; Burke, K.; Ernzerhof, M. *Phys. Rev. Lett.* **1996**, *77*, 3865−3868.
(26) Erhart, P.; Klein, A.; Åberg, D.; Sadigh, B. *Phys. Rev. B: Condens. Matter Mater. Phys.* **2014**, *90*, 035204.
(27) Neugebauer, J.; Scheffler, M. *Phys. Rev. B: Condens. Matter Mater. Phys.* **1992**, *46*, 16067−16080.
(28) Sinai, O.; Kronik, L. *Phys. Rev. B: Condens. Matter Mater. Phys.* **2013**, *87*, 235305.
(29) Fishman, M.; Zhuang, H. L.; Mathew, K.; Dirschka, W.; Hennig, R. G. *Phys. Rev. B: Condens. Matter Mater. Phys.* **2013**, *87*, 245402.
(30) Mathew, K.; Sundararaman, R.; Letchworth-Weaver, K.; Arias, T. A.; Hennig, R. G. *J. Chem. Phys.* **2014**, *140*, 084106.
(31) Gajdoš, M.; Hummer, K.; Kresse, G.; Furthmüller, J.; Bechstedt, F. *Phys. Rev. B: Condens. Matter Mater. Phys.* **2006**, *73*, 045112.
(32) Sun, Y.; Pignatello, J. J. *Environ. Sci. Technol.* **1995**, *29*, 2065−2072.
(33) Grabner, L. *Phys. Rev.* **1969**, *177*, 1315−1323.
(34) Herman, I. P. *Optical Diagnostics for Thin Film Processing*; Academic Press, Inc.: San Diego, CA, 1996.
(35) McIntyre, J. D. E.; Aspnes, D. E. *Surf. Sci.* **1971**, *24*, 417−434.

DOI: 10.1021/jacs.6b09550
J. Am. Chem. Soc. 2017, 139, 1830−1841

(36) Shayduk, R.; Herzog, M.; Bojahr, A.; Schick, D.; Gaal, P.; Leitenberger, W.; Navirian, H.; Sander, M.; Goldshteyn, J.; Vrejoiu, I.; Bargheer, M. *Phys. Rev. B: Condens. Matter Mater. Phys.* **2013**, *87*, 184301.
(37) Fano, U. *Phys. Rev.* **1961**, *124*, 1866−1878.
(38) Janotti, A.; Varley, J. B.; Choi, M.; Van de Walle, C. G. *Phys. Rev. B: Condens. Matter Mater. Phys.* **2014**, *90*, 085202.
(39) Sponza, L.; Véniard, V.; Sottile, F.; Giorgetti, C.; Reining, L. *Phys. Rev. B: Condens. Matter Mater. Phys.* **2013**, *87*, 235102.
(40) Mochizuki, S.; Fujishiro, F.; Minami, S. *J. Phys.: Condens. Matter* **2005**, *17*, 923.
(41) Green, M. *J. Chem. Phys.* **1959**, *31*, 200−203.
(42) De Gryse, R.; Gomes, W. P.; Cardon, F.; Vennik, J. *J. Electrochem. Soc.* **1975**, *122*, 711−712.
(43) Uosaki, K.; Kita, H. *J. Electrochem. Soc.* **1983**, *130*, 895−897.
(44) Cooper, G.; Turner, J. A.; Parkinson, B. A.; Nozik, A. J. *J. Appl. Phys.* **1983**, *54*, 6463−6473.
(45) Ramasesha, K.; De Marco, L.; Mandal, A.; Tokmakoff, A. *Nat. Chem.* **2013**, *5*, 935−940.
(46) Fecko, C. J.; Loparo, J. J.; Roberts, S. T.; Tokmakoff, A. *J. Chem. Phys.* **2005**, *122*, 054506.
(47) Asbury, J. B.; Steinel, T.; Stromberg, C.; Corcelli, S. A.; Lawrence, C. P.; Skinner, J. L.; Fayer, M. D. *J. Phys. Chem. A* **2004**, *108*, 1107−1119.
(48) Bakker, H.; Bonn, M.; Fayer, M. *Femtosecond Vibrational Spectroscopy of Aqueous Systems*; CRC Press: Boca Raton, FL, 2013.
(49) Lock, A. J.; Bakker, H. J. *J. Chem. Phys.* **2002**, *117*, 1708−1713.
(50) Eftekhari-Bafrooei, A.; Borguet, E. *J. Am. Chem. Soc.* **2010**, *132*, 3756−3761.
(51) Cheng, J.; VandeVondele, J.; Sprik, M. *J. Phys. Chem. C* **2014**, *118*, 5437−5444.
(52) Kolesov, G.; Grånäs, O.; Hoyt, R.; Vinichenko, D.; Kaxiras, E. *J. Chem. Theory Comput.* **2016**, *12*, 466−476.
(53) Harriman, A.; Pickering, I. J.; Thomas, J. M.; Christensen, P. A. *J. Chem. Soc., Faraday Trans. 1* **1988**, *84*, 2795−2806.

DOI: 10.1021/jacs.6b09550
J. Am. Chem. Soc. 2017, 139, 1830−1841